Computational Modeling of Flexible Biodegradable Films with Engineered Defects

Rachel Waxman
Mechanical and Nuclear Engineering
Virginia Commonwealth University
Richmond, VA, USA
waxmanr@vcu.edu

Ibrahim Guven
Mechanical and Nuclear Engineering
Virginia Commonwealth University
Richmond, VA, USA
iguven@vcu.edu

Vamsi K Yadavalli
Chemical and Life Science Engineering
Virginia Commonwealth University
Richmond, VA, USA
vyadavalli@vcu.edu

***Abstract*— A new material model within the peridynamic framework was implemented to study the deformation and failure of flexible biodegradable films with engineered defects. The new approach was demonstrated by performing peridynamic simulations of a structure under tension with a number of defect (slit) configurations. The simulations were first performed without allowing failure in the material to study deformation patterns. The failure patterns were then examined for two different critical stretch values. The effects of horizontal and vertical spacing values separating the slits, and slit arrangements were identified. This study demonstrated the suitability of peridynamic approach for parametric studies of structures with manufactured defects.**

Keywords—peridynamics, kirigami, flexible biodegradable films, engineered defects, fracture, failure.

I. INTRODUCTION

Flexible and thin-film devices are of great interest in the area of ubiquitous biosensing and bioelectronics. Such systems can include human-machine interfaces, soft robotics, implantable devices and engineered tissues for regenerative medicine. Multifunctional materials can establish adaptive and flexible interfaces with the body [1, 2]. Forming flexible, compliant, thin, yet mechanically robust interfaces to achieve these functions is an ongoing challenge. As an example, various wearables and implantable devices have been envisioned for the monitoring of health and wellness. In order to drive these devices, new forms of power sources with properties of flexibility, miniaturization, and biocompatibility are needed. Integrating biocompatibility and biodegradation can vastly expand the scope of synthetic skins for applications in the areas of biohybrid systems, soft matter electronics, prosthetics, wound healing, and health monitoring. An increasing challenge involves reducing *e-waste*, which involves adapting sustainable materials and processes, while reinterpreting the product lifecycle of such devices [3].

Various polymeric composites have been used to form electronic skins, energy harvesters, and stretchable electronics in soft and dynamic 3D environments. Structural design concepts, and strategies such as meshes, cracks, prestressing, buckling, and serpentine architectures have been proposed to impart functional conformability [4]. Of recent interest are kirigami inspired architectures that can provide a unique opportunity for stretchability, bendability and thus conformability. While designed to enhance elasticity for traditionally stiff materials, kirigami architectures can transform intrinsically flexible and soft materials in interesting ways [5]. Materials can exhibit deformability beyond the strain limits of pristine materials, allowing for multifunctionality e.g. stretchability, conformability to complex interfaces, conductivity, fault tolerance, biocompatibility, or reconfigurability. Out-of-plane deformations can enable reversible geometry changes, transforming between planar 2D and 3D [6, 7]. Using computational tools, it is possible to predict and thereby precisely engineer, the operative behaviors under mechanical stresses.

Kirigami cuts/patterns have been shown on various materials such as polymers and paper. However, the use of degradable biopolymers has not been investigated [6, 8]. In recent work (*under review*), we have developed a new approach to induce stretchability and mechanical conformability via kirigami-inspired cuts in silk protein sheets. Silk proteins form a versatile class of bioresorbable, degradable biomaterials with uses in drug delivery, nanostructured scaffolds, and recently, in implantable bioelectronics, bio-integrated devices, and as platforms for transistors, solar cells and photonic devices [9]. Here, the microfabrication of flexible, optically transparent, silk fibroin kirigami films is realized using a light-reactive silk protein with a facile photolithographic process (Fig. 1). We utilize "protein lithography" via photoreactive silk fibroin as a route to multiscale fabrication [10, 11]. Material subtraction or cutting is photolithographically accomplished in a single step process. The biomaterial behaves as a negative-tone photoresist, crosslinking under UV irradiation. This results in flexible, free-standing, optically transparent, macroscale biomaterial sheets with precisely defined microscale cuts. The cuts have a high structural fidelity and spatial resolution to form micropatterns over large areas. SEM imaging shows ordered patterns of various complexities over a large area (cm scale) of flexible fibroin sheet (Fig. 2). The microscale kirigami films are mechanically robust and can be held, rolled or bent into various conformations numerous times without any loss in their

2377-5726/20/$31.00 ©2020 IEEE
DOI 10.1109/ECTC32862.2020.00138

physico-chemical-mechanical properties. They are optically transparent enabling potential use in stretchable optics and transparent devices [12]. A computational approach can be used to better design these materials/devices.

This study uses peridynamic theory [13, 14] to develop simulations of deformation and failure of such sheets under various mechanical loading conditions. Our goal is to understand the properties of biomaterial sheets with rationally designed-kirigami patterns in order to achieve flexible, multifunctional materials with unique mechanical properties. Inherently, these devices are expected to be subjected to large deformations and to experience considerable out-of-plane displacements. Prediction of failure initiation and propagation through computational simulations has been an important research area. Most of such studies involve finite element analysis (FEA), which is a well-established and robust numerical method. However, it is based on the solution of partial differential equations (PDEs) of classical continuum mechanics, which suffers from the inherent limitation that the spatial derivatives do not exist at geometric discontinuities such as crack tips, crack surfaces or along material interfaces. Peridynamic approach allows failure initiation and propagation at multiple locations in the body with arbitrary paths. Further, the material interfaces have their own mechanical properties. Peridynamic theory is naturally able to capture large deformations.

By coupling the biocomposites with these stretchable substrates, previously unattained out-of-plane bending and high surface areas can be achieved. Kirigami based structural designs can lead to dynamic shaping of stretchable and foldable structures. For instance, rational design can provide a method to release of applied strain through geometry changes without changes in the materials themselves. Kirigami sheets possess a mechanical regime in which sheets are highly stretchable and very soft in comparison to pristine (uncut) sheets. This can also be associated to the out-of-plane deformations. This regime can start after a transition from an initial less soft regime governed by in-plane deformations. Thus the extreme softness of the kirigami structure could emerge as a result of a transition from the 2D to 3D deformation. In order to precisely engineer the films for various applications, it is important to understand their mechanical behavior under different strains and as a function of the cut geometry. Interestingly, by bending the films, certain patterns (e.g. branches, saddles, or chevrons) result in opening and out-of-plane deformations that can be exploited. Cuts down to ~10 μm using benchtop lithography can be formed. Partial cuts, particularly at smaller feature sizes, could be formed by reducing the time of crosslinking. This results in films that can potentially have engineered weakness along the patterns, such as wrinkles.

The introduction of deformability in the kirigami sheets, with the fracture resistant cuts opening to accommodate stretch allows highly conformable interfaces or attachment at interfaces. The current study aims to demonstrate a computationally guided design approach to tune flexibility in biocompatible and biodegradable devices. Peridynamic approach's ability to capture the deformation and failure modes is demonstrated by considering a thin sheet with various engineered defect configurations under tensile loading. Deformation with and without failure is examined to identify trends.

II. Methods

A. Fabrication Process

Silk fibroin is photolithographically patterned in a single step process, in a form that simulates material removal or cuts. Initially, a solution of photocrosslinkable (silk) fibroin in hexafluoroisopropanol (HFIP) with a UV photoinitiator was cast on a plain glass slide and crosslinked by exposure under 365 nm UV light (Fig. 1) through a photomask with the "cut" design darkened. The cuts remain uncrosslinked and can be developed (1M LiCl in DMSO), resulting in a crosslinked fibroin sheet that can be easily peeled off when immersed in water. As a scalable process, cuts down to a few μm can be easily formed over large areas (cm) on flexible films. The crosslinked fibroin sheets formed are water insoluble and stable in a wide range of solvents. They are optically transparent and can be formed with ordered patterns of various complexities over large areas (cm scale) of flexible silk fibroin sheets..

B. Peridynamic Approach

The peridynamic approach was introduced by [13] in order to better address failure initiation and propagation in solids. This was achieved by writing the governing differential equations of classical continuum mechanics in the form of integral equations. The resulting integral equations are written at a material point inside the solid body; they sum up the effects of the force field acting on it exerted by other material points in its neighborhood. This neighborhood is defined by a finite distance, which is called *horizon*, which in turn introduces non-locality to the treatment of the problem. The force acting on a material point is then related to its mass density and acceleration. The solid body is discretized into smaller subdomains with a material point at the center, representing all of the solid matter within this finite volume of the sub-domain. Each material point interacts with other material points in its vicinity (aka *family*) defined by the horizon. The approach and various implementations are described in great detail in [13-15].

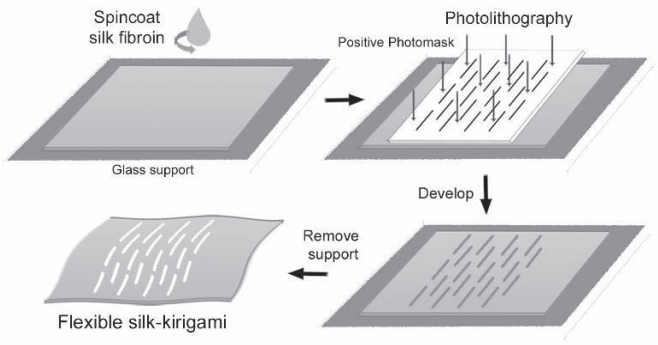

Fig. 1. Schematic of photolithographic fabrication of flexible sheets with kirigami-inspired cuts.

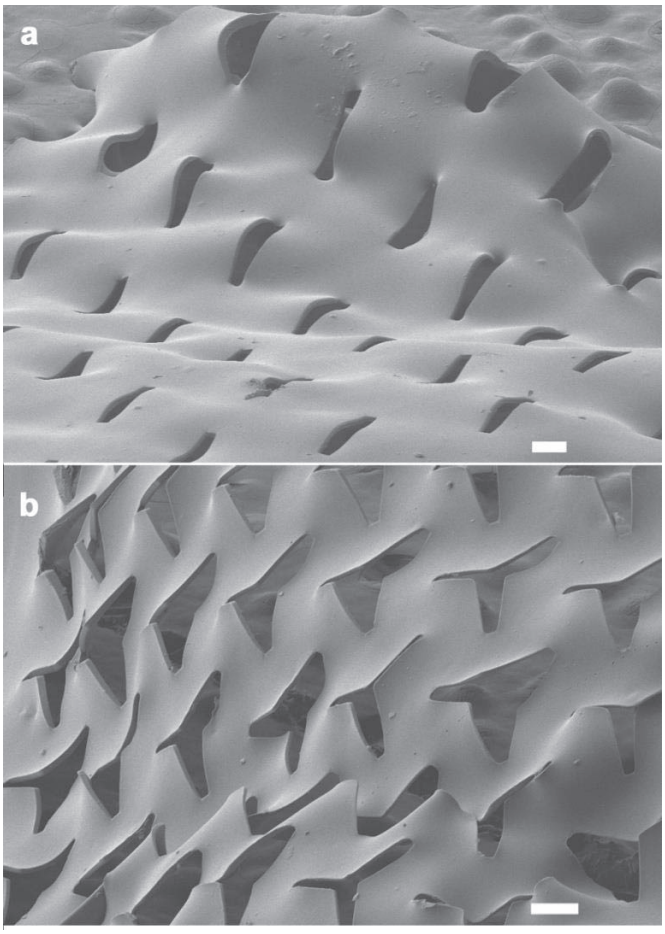

Fig. 2. Various microscale designs can be easily fabricated (a) slits and (b) Y-shaped cuts. Scale bar on both panels = 100 μm..

The unique feature of peridynamic approach is its ability to represent realistic failure initiation and propagation behaviors observed in experiments [16-19]. At the beginning of a computational simulation, each material point has a complete family with individual intact force interactions with each other material point in its family. As the simulation progresses, deformation occurs due to applied boundary and initial conditions. In a deformed neighborhood, material points move towards (contraction) or away (elongation) from each other. The ratio between the elongation (i.e., added length) and the original distance is called *stretch* in peridynamic framework. There is a critical stretch, s_{cr}, above which two material points cease to interact whose value depends on the critical energy release rate or fracture toughness of the material [20]. Once an interaction between two material points is terminated due to exceeding critical stretch, the force carried by the broken interaction is redistributed to the neighboring interactions, which may lead to additional interaction terminations. The ratio between the number of terminated interactions to the initial number of interactions at a material point is termed *damage*. Initially damage at a material point is zero. As interaction terminations accumulate, its value increases with a possible maximum of unity, which means the material point has lost all of its initial interactions.

Early implementations of peridynamic approach considered a linear relationship between the force density and stretch between material points. Current work presents a new peridynamic material model that is suitable for simulating the behavior of silk fibroin [21]. In this model, in a stress-strain (or an equivalent force density-stretch) relationship, an initial stiff response is followed by a plateau that has much less stiffness; there may or may not be a secondary stiffening at high deformations prior to ultimate failure. The current peridynamic implementation considers piecewise linear response defined by three straight lines (red dashed lines in Fig. 3) with the gray curve representing the continuous nonlinear response that may be exhibited by the material.

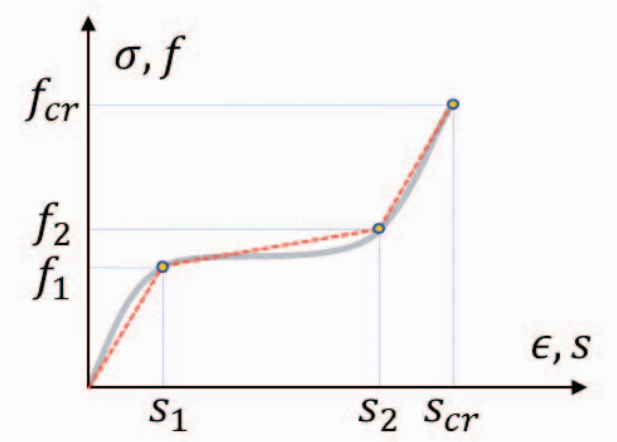

Fig. 3. A peicewise linear stress-strain response.

III. Peridynamic Analysis

The peridynamic approach is demonstrated for the material behavior shown in Fig. 3 by considering a rectangular structure under tensile loading. A total of 15 geometric configurations with different engineered defects (slits) were considered; the 16th case is a structure with no defect. A representative geometry for cases 1-9 is shown in Fig. 4 with a width $W = 700\ \mu m$, a height $H = 900\ \mu m$, and a depth of 60 μm (not shown). There are 13 slits in the structure, each with length $l = 120\ \mu m$, and thickness of 20 μm, arranged in 5 rows (number of slits in each row: 3-2-3-2-3). The slits are separated from each other horizontally by a distance of Δx and vertically by a distance of Δy values of which are tabulated in Table 1. Schematic representations of cases 1-9 are shown in Fig. 5.

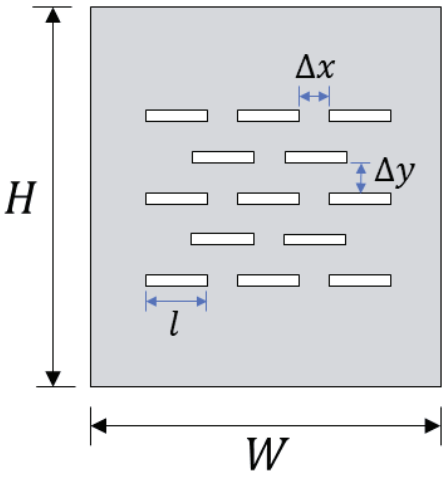

Fig. 4. Geometric parameters of peridynamic models of cases 1-9.

TABLE I. HORIZONTAL AND VERTICAL SPACINGS IN CASES 1-9

Case #	Δx (μm)	Δy (μm)
1	20	20
2	40	20
3	60	20
4	20	40
5	40	40
6	60	40
7	20	60
8	40	60
9	60	60

In addition to the 9 cases described above, six more cases (10-15) were examined for the effects of slit length and width of rows 2 and 4 as schematically presented in Fig. 6. It is worth noting that all 15 cases have the same amount of *total* slit length as well as the number of rows. Case 10 assigns a single slit per row. Cases 11 and 12 have the same end-to-end footprint for each row but using increasingly smaller individual slit lengths (i.e., individual slit lengths in case 12 is smaller than case 11). Cases 13-15 were designed such that the rows 2 and 4 start and end at the same horizontal coordinates as the rows 1, 3 and 5 while maintaining the same total slit length. Cases 9, 11, and 12 are directly comparable to cases 13, 14, and 15, respectively in that each pair has identical rows 1, 3, and 5 while their rows 2 and 4 are altered in slit arrangement.

The peridynamic model used a regular grid with spacing 5 μm. The base case with no slits (case 16) yields a peridynamic model with 302,400 material points. With the material points corresponding to the slits removed, cases 1-15 possess 301,152 material points. In all cases, the structure was subjected to initial uniform tensile strain of 30% in the vertical direction; the top and bottom horizontal boundaries were then held in place for the remainder of the simulation.

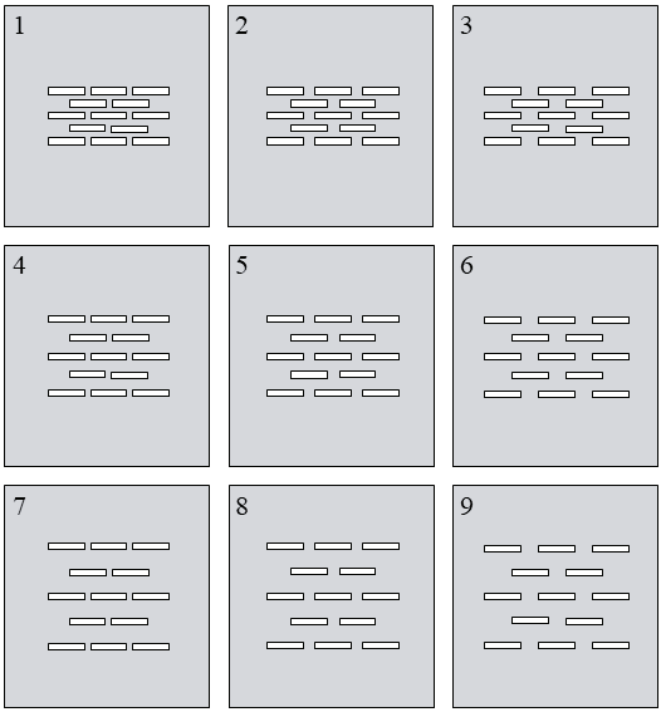

Fig. 5. Slit configurations of peridynamic models of cases 1-9.

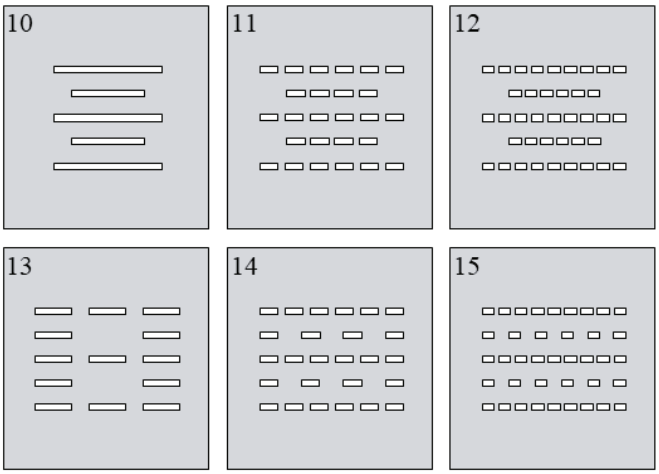

Fig. 6. Slit configurations of peridynamic models of cases 10-15.

IV. RESULTS

Three different groups of peridynamic simulations were performed. In the first group, the models were not allowed to fail allowing the deformation patterns to be examined, and quantifying *stretchability*. The next groups of simulations allowed failure to take place at different critical stretch values leading to examination of failure patterns.

A. Deformation Patterns and Stretchability

The peridynamic simulations were performed with the initial condition of uniform 30% strain in the vertical direction and the boundary conditions of permanent hold of the top and bottom horizontal boundaries. The simulations progressed until the system equilibriated; presence of slits requires this equilibriation

process. A horizontal plane away from the slits and the boundaries was placed to monitor the total force in the vertical direction in order to verify equilibriation of the system. The value the force converges to is an indication of stretchability. For a given applied global strain field (30% in this work), if the force that is required to hold the system in place is lower, it indicates higher stretchability, and vice versa.

The deformed shapes under static equilibrium for cases 1-9 and 10-15 are shown in Figs. 7 and 8, respectively; the contour colors indicate vertical displacement. The deformed shapes of the slits display an interesting trend: with the exception of case 10, all other cases have identical individual slit lengths within each case while displaying a great variability in their deformed shapes. For example, in cases 1-6 and 13, there are large differences in slit deformed shapes (largely horizontal to diamond shapes). Conversely, in cases 7, 8, 9, 11, and 12, the deformed shapes of slits remained similar. Cases 14 and 15 appear to be in between the aforementioned classifications. Another interesting observation is that the arrangement of slits may lead to disproportionate deformation among the slits. The starkest example is seen in case 10 in which the lists in rows 2 and 4 are shielded from deformation by the slits in rows 1, 3 and 5 that are excessively deformed. Similar patterns, to a lesser degree, are seen in cases 13-15.

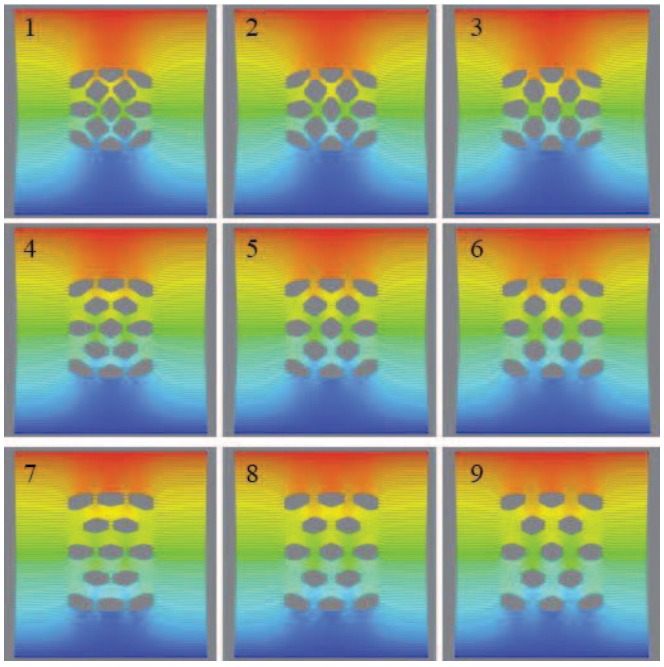

Fig. 7. Deformed shapes of cases 1-9 when no failure is allowed.

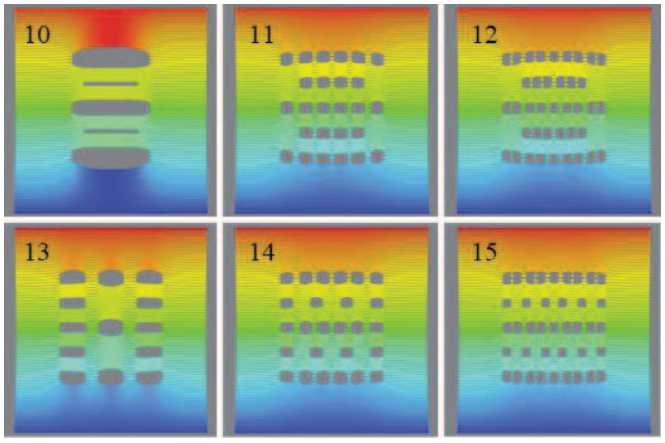

Fig. 8. Deformed shapes of cases 10-15 when no failure is allowed.

Stretchability of each configuration is quantified by recording the total vertical internal force developed by undergoing the deformations. As mentioned earlier, an additional case with no slits, case 16, was considered as a base case with the internal vertical total force F^*. The ratio of vertical internal total force, F, in cases 1-9 to that of the case 16 are plotted to quantify the reduction in vertical force by introduction of slits (Figs. 9 and 10). In all 9 cases, the force decreased to between 58% to 67% of the no-slit case. When the vertical spacing between the slits is kept constant, increasing the horizontal spacing increased stretchability (Fig. 9). Similarly, when the horizontal spacing is kept constant, decreasing the vertical spacing increased stretchability (Fig. 10). The force ratios associated with the cases 10-15 along with case 9 are plotted in Fig. 11. Except for case 10, the new cases yield lower stretchability. Following is the stretchability ranked in all 15 cases, from high to low: 3-6-2-9-5-10-8-1-4-7-13-12-11-14-15.

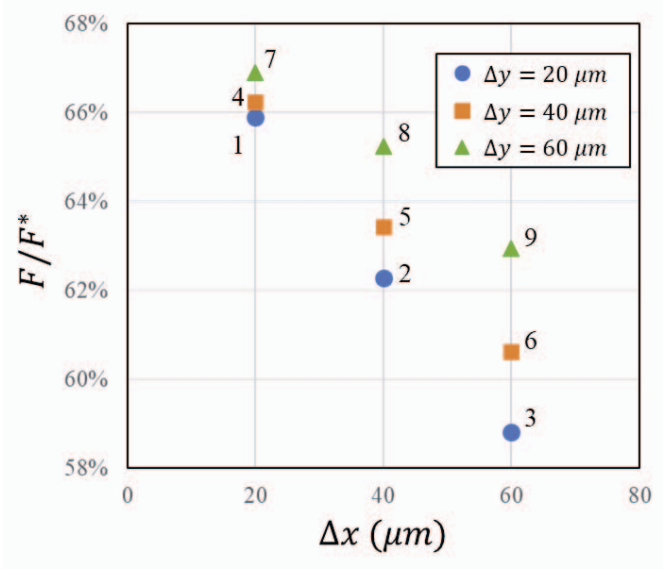

Fig. 9. Effect of horizontal spacing, Δx, on stiffness of the structure.

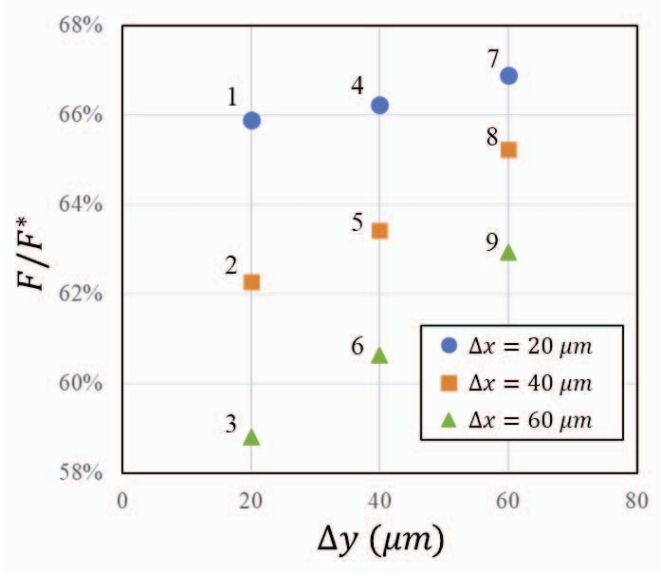

Fig. 10. Effect of vertical spacing, Δy, on stiffness of the structure.

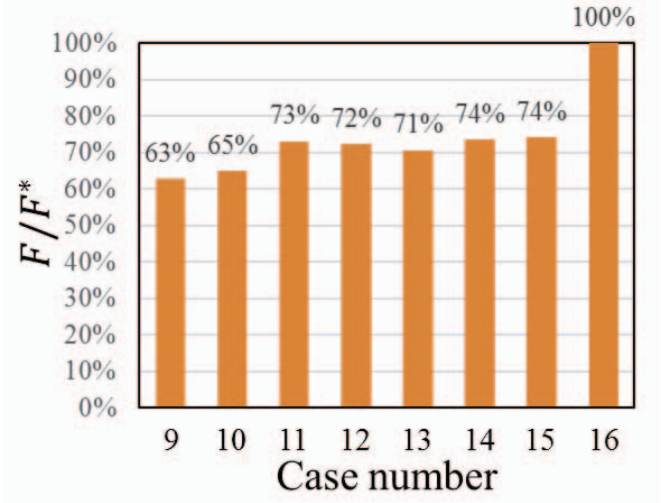

Fig. 11. Effect of vertical spacing, Δy, on stiffness of the structure.

B. *Failure Patterns*

The peridynamic models were simulated for all 15 cases with failure allowed to initiate and propagate. This is done two separate times with different critical stretch values to examine interaction between the geometric configuration and material strength. The first set of results were obtained by using critical stretch value of 0.636, and the second set used a value of 0.7314. The failure patterns corresponding to the first set are presented in Figs. 12 and 13. The higher critical stretch results are given in Figs. 14 and 15.

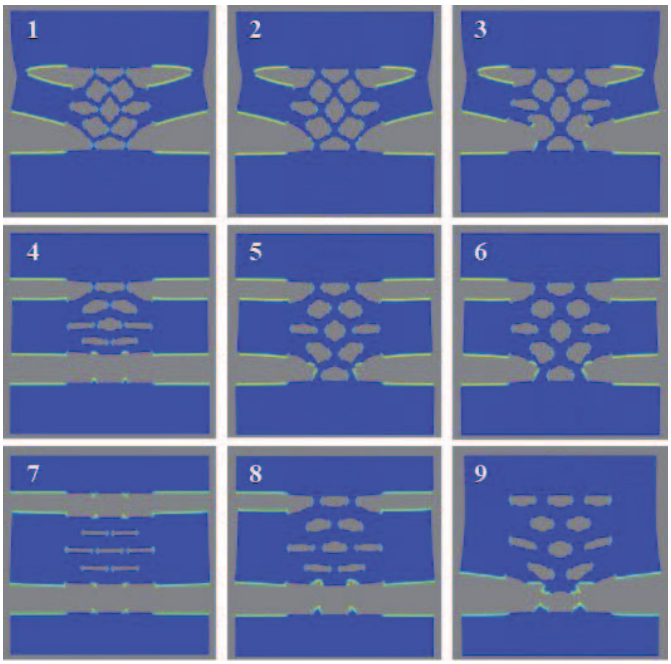

Fig. 12. Failure modes of cases 1-9 when critical stretch, s_{cr}, is 0.636.

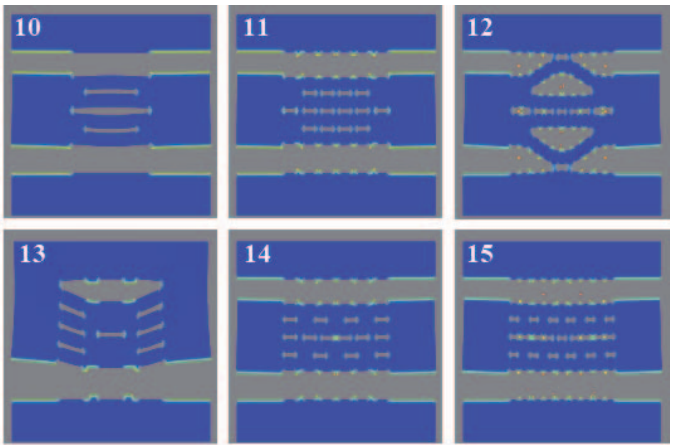

Fig. 13. Failure modes of cases 10-15 when critical stretch, s_{cr}, is 0.636.

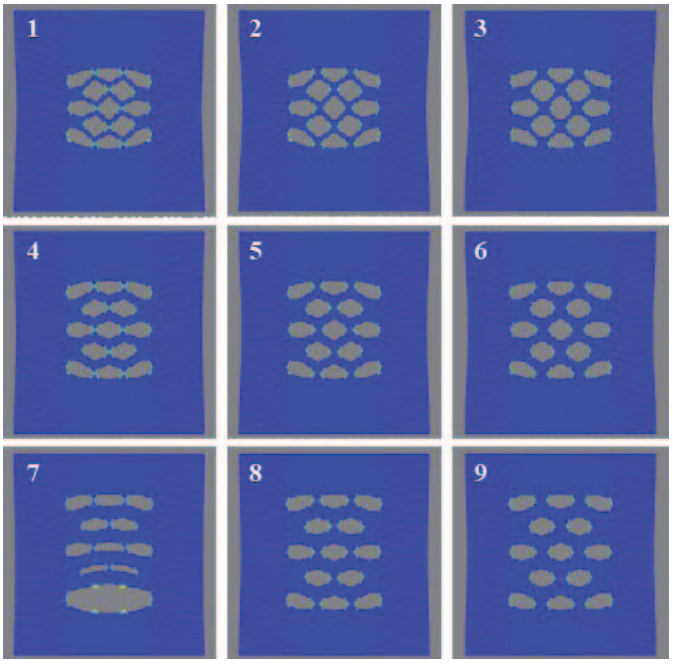

Fig. 14. Failure modes of cases 1-9 when critical stretch, s_{cr}, is 0.7314.

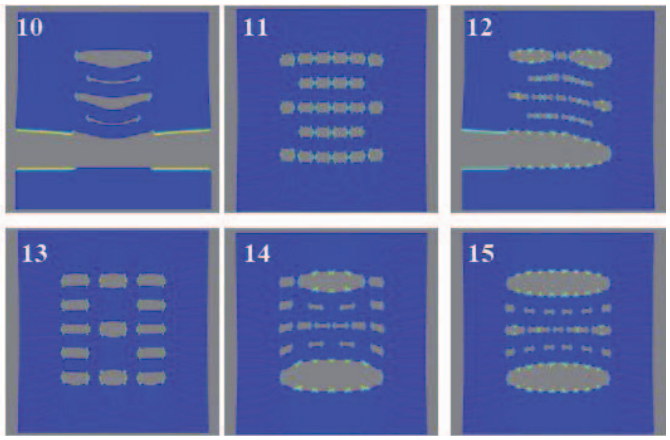

Fig. 15. Failure modes of cases 10-15 when critical stretch, s_{cr}, is 0.7314.

Examination of Figs. 12-15 allows for classification of failure patterns, in broad strokes, into five main categories:

a. There are 2 full horizontal fractures

b. There is 1 full horizontal fracture and significant fracture and damage elsewhere

c. There is 1 full horizontal fracture and no significant damage and failure elsewhere

d. There is no full horizontal fracture but there is significant damage and failure

e. There is neither full horizontal fracture nor significant damage and failure

Based on the above classifications, the results presented in Figs. 12-15 the categories for each case using each critical stretch value are listed in Table II.

When critical stretch is 0.636, six of the 15 cases were able to not develop a full horizontal crack. Cases 7, 10, 11, 14, and 15 developed 2 full horizontal cracks (category a) while cases 4, 8, and 13 developed 1 full horizontal crack with also significant damage elsewhere (category b). Case 9 appears to be on the border of the threshold from no full horizontal crack to having one (category c). The remaining cases (1, 2, 3, 5, 6, and 12) are of category d in which there is no full horizontal fracture but there is significant damage and failure.

In the next set of peridynamic simulations that used a 25% higher critical stretch, 0.7314, only one case (10) developed a full horizontal crack. The remaining cases were either category d (7, 12, 14, and 15) or category e (1-6, 8, 9, 11, and 13).

TABLE II. FAILURE PATTERN CLASSIFICATIONS FOR ALL CASES

Case #	$s_{cr} = 0.636$	$s_{cr} = 0.7314$
1	d	e
2	d	e
3	d	e
4	b	e
5	d	e
6	d	e
7	a	d
8	b	e
9	c	e
10	a	c
11	a	e
12	d	d
13	b	e
14	a	d
15	a	d

The cases can also be ranked within each critical stretch scenario based on their resistance to fracture by observing Figs. 12-15. The rankings from best performance to worst performance for scenario 1 ($s_{cr} = 0.636$) and scenario 2 ($s_{cr} = 0.7314$) are

Scenario 1: [2-6]-[1-5]-3-12-9-13-[8-4]-[7-11-14-15-10]

Scenario 2: [9-6-13]-[5-8-3-2]-[1-4-11]-7-[14-15]-12-10

in which the cases enclosed within square brackets are considered to be ranked equally. Notably, the cases 9, 13 and 8 ranked better in scenario 2 while case 12 dropped significantly in its ranking.

V. DISCUSSION

This study presented a new material model within the peridynamic framework that was implemented to further understand the deformation and failure of flexible biodegradable films with engineered defects. Peridynamic simulations of a structure under tension with a number of defect (slit)

configurations were performed for demonstration of the new approach. Simulations considered both deformation without failure and with failure. When studying the failure patterns, two scenarios of critical stretch values were used. The effects of horizontal and vertical spacings separating the slits were identified. These results are preliminary in nature. This study demonstrated the suitability of peridynamic approach for parametric studies of structures with manufactured defects. Figure 16 (top) shows an optical microscopy image of such a structure with partial failure; one of the peridynamic simulations in the current work shows similar failure patterns (Fig. 16 – bottom). The follow on work consists of quantitative comparison against experiments and studying the out-of-plane deformation in the context of wrapping of thin films around three-dimensional bodies (conformability).

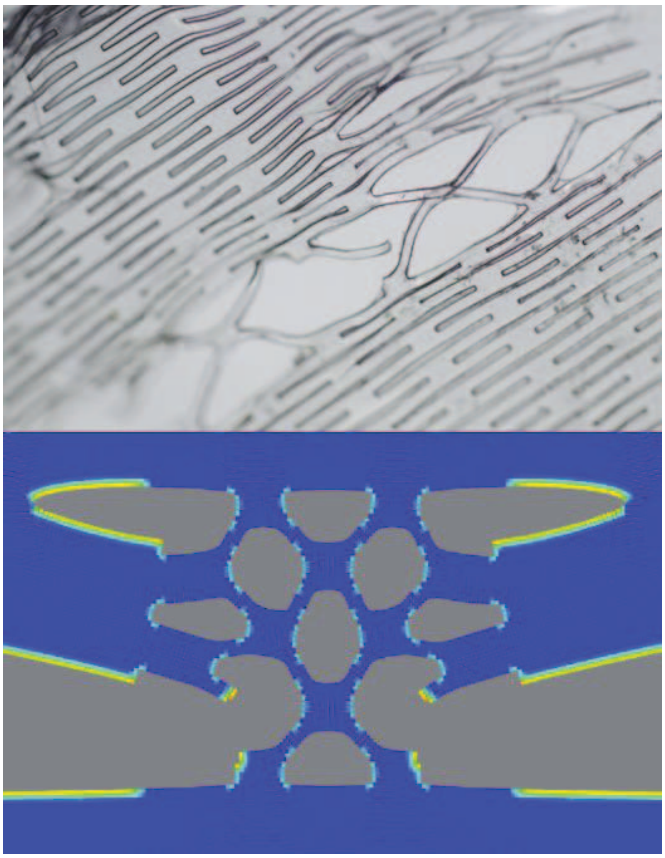

Fig. 16. Top: optical microscopy imaging of failure of the sheets under tensile stress, and bottom: peridynamic simulation (case 3) with critical stretch 0.636.

ACKNOWLEDGEMENTS

VKY acknowledges support from NSF-CBET-1704435

REFERENCES

1. Chortos, A., J. Liu, and Z. Bao, Pursuing prosthetic electronic skin. Nature materials, 2016. 15(9): p. 937.
2. Someya, T., Z. Bao, and G.G. Malliaras, The rise of plastic bioelectronics. Nature, 2016. 540(7633): p. 379.
3. Irimia-Vladu, M., "Green" electronics: biodegradable and biocompatible materials and devices for sustainable future Chemical Society Reviews, 2014. 43(17): p. 588.
4. Matsuhisa, N., et al., Materials and structural designs of stretchable conductors. Chemical Society Reviews, 2019. 48(11): p. 2946-2966.
5. Chen, B.G.-g., et al., Topological mechanics of origami and kirigami. Physical review letters, 2016. 116(13): p. 135501.
6. Xu, L., T.C. Shyu, and N.A. Kotov, Origami and kirigami nanocomposites. Acs Nano, 2017. 11(8): p. 7587-7599.
7. Vachicouras, N., et al., Engineering reversible elasticity in ductile and brittle thin films supported by a plastic foil. Extreme Mechanics Letters, 2017. 15: p. 63-69.
8. Ning, X., et al., Assembly of Advanced Materials into 3D Functional Structures by Methods Inspired by Origami and Kirigami: A Review. Advanced Materials Interfaces, 2018. 5(13): p. 1800284.
9. Omenetto, F.G. and D.L. Kaplan, New Opportunities for an Ancient Material. Science, 2010. 329(5991): p. 528-531.
10. Kurland, N.E., et al., Precise Patterning of Silk Microstructures Using Photolithography. Advanced Materials, 2013. 25(43): p. 6207-6212.
11. Xu, M., et al., Easy, Scalable, Robust, Micropatterned Silk Fibroin Cell Substrates. Advanced Materials Interfaces, 2019: p. 1801822.
12. Kim, K., et al., Recent Advances in Transparent Electronics with Stretchable Forms. Advanced Materials, 2019. 31(20): p. 1804690.
13. Silling, S.A., Reformulation of elasticity theory for discontinuities and long-range forces. Journal of the Mechanics and Physics of Solids, 2000. 48(1): p. 175-209.
14. Silling, S.A., et al., Peridynamic states and constitutive modeling. Journal of Elasticity, 2007. 88(2): p. 151-184.
15. Madenci, E., & Oterkus, E. (2014). Peridynamic theory and its applications. New York: Springer.
16. Waxman, R., & Guven, I. (2019). An experimental and peridynamic study of the erosion of optical glass targets due to sand and sphere microparticles. Wear, 428, 340-355.
17. Baber, F., & Guven, I. (2017). Solder joint fatigue life prediction using peridynamic approach. Microelectronics Reliability, 79, 20-31.
18. Baber, F., Ranatunga, V., & Guven, I. (2018). Peridynamic modeling of low-velocity impact damage in laminated composites reinforced with z-pins. Journal of Composite Materials, 52(25), 3491-3508.
19. Dereure, Corentin, et al. "Laser induced dynamic fracture of fused silica: Experiments and simulations." Journal of Non-Crystalline Solids 511 (2019): 125-139.
20. Silling, Stewart A., and Ebrahim Askari. "A meshfree method based on the peridynamic model of solid mechanics." Computers & structures 83.17-18 (2005): 1526-1535.
21. Yoshioka, Taiyo, et al. "A study of the extraordinarily strong and tough silk produced by bagworms." Nature communications 10.1 (2019): 1-11.